Boundary-Layer Meteorol (2010) 136:457–487
DOI 10.1007/s10546-010-9511-2

ARTICLE

Experimental Study of Pollutant Dispersion Within a Network of Streets

Valeria Garbero · Pietro Salizzoni · Lionel Soulhac

Received: 11 November 2009 / Accepted: 18 May 2010 / Published online: 4 June 2010

Abstract We investigate the dispersion of a passive scalar within an idealised urban district made up of a building-like obstacle array. We focus on a street network in which the lateral dimension of the buildings exceeds the street width, a geometry representative of many European cities. To investigate the effect of different geometries and wind directions upon the pollutant dispersion process, we have performed a series of wind-tunnel experiments. Concentration measurements of a passive tracer have enabled us to infer the main features characterising its dispersion within the street network. We describe this by focusing on the roles of different transfer processes. These are the channelling of the tracer along the street axes, the mixing at street intersections, and the mass exchange between the streets and the overlying atmospheric flow. Our experiments provide evidence of the dependence of these processes on the geometrical properties of the array and the direction of the overlying atmospheric flow.

Keywords Network of streets · Obstacle array · Street canyon · Urban air pollution · Wind-tunnel experiments

1 Introduction

Air pollution and the potential risks associated with continuous or accidental releases of toxic material in the urban environment motivate the study of pollutant dispersion within

---

V. Garbero (✉)
Dipartimento di Matematica, Politecnico di Torino, Corso Duca degli Abruzzi 24, 10129 Torino, Italy
e-mail: valeria.garbero@polito.it

V. Garbero
Golder Associates S.r.l., Via Banfo 43, 10155 Torino, Italy

P. Salizzoni · L. Soulhac
Laboratoire de Mécanique des Fluides et d'Acoustique, Université de Lyon, CNRS, Ecole Centrale de Lyon, INSA Lyon, Université Claude Bernard Lyon I, 36, avenue Guy de Collongue, 69134 Ecully, France

small-scale urban-type geometries such as street canyons, street intersections and obstacle arrays. The presence of buildings and their arrangement significantly affects the flow field and mass exchange mechanisms and results in extremely complex dispersion patterns. A common approach to investigate these phenomena is to analyse the dispersion through idealised urban geometries. Although these geometries necessarily simplify the real urban environment, a reduction of complexity is essential so as to focus on the physical mechanisms governing the flow dynamics and the pollutant dispersion.

Several studies on pollutant dispersion in urban areas have focussed on the street scale by adopting these simplified geometries. Most of the existing literature investigates street canyons with an external wind direction perpendicular to the axis of the street, in order to clarify the influence of different dynamical and geometrical parameters on the flow and hence the pollutant dispersion. Among these studies we cite the recent works of Assimakopoulos et al. (2003) on the influences of canyon geometry, Salizzoni et al. (2009a) and Solazzo et al. (2008) on the role of the external atmospheric and traffic induced turbulence respectively, Gromke and Ruck (2007) on the effects of trees within the canyon, and Sini et al. (1996) on the influence of solar induced heating of the canyon walls. Some studies have looked at street intersections (Hoydysh et al. 1995; Soulhac et al. 2009) investigating the flow patterns and dispersion processes within them.

At the larger district scale (Britter and Hanna 2003), several studies have focussed on sparse and regular buildings, usually referred to as ‘groups of obstacles’. Flow and dispersion characteristics in small-scale domains have been studied experimentally by several authors. Davidson et al. (1995, 1996) performed field investigations and wind-tunnel simulations to study the near-field behaviour of plumes in relatively sparse cube arrays. The plume spreading was defined as a function of two key parameters controlling the flow regimes within the array and the dispersion characteristics. These are porosity factors, namely the plan and frontal area density of the buildings, usually referred to as λ_P and λ_F respectively (Grimmond and Oke 1999). MacDonald et al. (1997, 1998) examined the effect of the plan area density λ_P on plume dispersion in a wind-tunnel and at a field site and expanded the study by considering different obstacle width-to-height ratios. In all of these experiments, the measured mean concentration profiles within the array were found to be in good agreement with Gaussian distribution profiles. Theurer et al. (1996) showed that in more irregular obstacle arrays a Gaussian plume model can approximately model the concentration distribution only in the far-field, at distances larger than a ‘radius of homogenization’, whereas in the near-field the dispersion depends strongly on the local arrangements of the obstacles. Recently, Gailis and Hill (2006) performed wind-tunnel simulations to investigate the dispersion of a tracer within a large array of obstacles simulating the large field study MUST (Mock Urban Setting Test) at the 1:50 scale (Yee and Biltoft 2004). The study demonstrates the physical mechanisms involved in the development of a dispersing plume within an urban-like environment and focusses on the spatial evolution of the mean and fluctuating concentrations within the array.

More recently, similar studies have exploited numerical simulations. Hanna et al. (2002) performed large-eddy simulations through the finite element flow solver FEFLO to investigate mean flow and turbulence within obstacle array configurations consisting of simple cubic elements. Coceal et al. (2006) performed direct numerical simulations of turbulent flow over regular arrays of urban-like cubic obstacles and studied the effects of the geometrical layout on the momentum transfer mechanisms between the canopy and the overlying flows. Santiago and Martilli (2007) used Reynolds-averaged Navier–Stokes numerical simulations to investigate wind flow and pollutant dispersion within and above a three-dimensional cubic array. The results, validated by wind-tunnel data, have been used to improve the understanding of the three-dimensional flow structure that is responsible for pollutant dispersion.

Almost all of these studies at the district scale involve low density obstacle arrays in the so-called 'wake interference regime' (Oke 1988), where the velocity field is characterised by the interaction between the wakes developing downwind of each obstacle. This occurs in geometries where the spacing between obstacles and their sizes are approximately equal and it is not possible to distinguish between a 'street' bounded by two obstacles and an 'intersection' connecting different streets. In this sense the geometries of these low density obstacle arrays are similar to that of North American cities or European suburban districts and very different from those characterising the central districts of most European cities, where the flow regime is much more similar to a 'skimming flow'. When the obstacles are densely packed and the width of the building blocks exceeds that of the streets separating them, the interaction between the flow developing in different regions of the domain is limited. In these cases we can therefore identify some properties of the velocity field that characterise the flow within a street and that clearly differentiate it from that developing at an intersection or square. Equally, we can quite easily identify the shear layer at the top of the street canyons as the boundary separating the flow within the urban canopy and the overlying atmospheric flow. We call this typical urban-type geometry a 'street network' (Soulhac 2000): a domain made up of streets connected via intersections and overlain by a mixing layer at the top whose dynamics govern the exchanges of momentum and mass with the overlying atmospheric flow.

The aim of the present study is to contribute to the understanding of the dispersion processes that take place in a street network and to analyse how they depend on the geometrical layout (street aspect ratio) and the wind direction. The study focuses on an idealised urban canopy, made up of regularly spaced obstacles with equal height, that represents a high simplification of the real urban geometry. However, given that many aspects of the problem remain poorly understood, this simplification is necessary in order to infer the main features characterising pollutant dispersion in street networks. Finally, it is worth noting that the street network geometry investigated here differentiates these experiments from those performed over other urban idealised geometries in the studies previously cited on pollutant dispersion within sparse obstacle arrays (Davidson et al. 1996; MacDonald et al. 1997, 1998; Gailis and Hill 2006). Therefore the results presented here provide additional information that complements existing datasets and which will be useful in evaluating the performances of numerical simulations and in validating operational dispersion models.

2 Experimental Set-Up and Measurement Techniques

Our experiments were performed in the atmospheric wind tunnel of the Laboratoire de Mécanique des Fluides et d'Acoustique of the Ecole Centrale de Lyon, France. This recirculating wind-tunnel measures 24 m in length, 7.4 m in height and 7.2 m in width and has a test section 14 m long, 2.5 m high and 3.7 m wide. A neutrally stratified boundary layer was generated by a row of spires and floor roughness elements (Irwin 1981). The spires were 500 mm high and the floor roughness consisted of nut-covered rectangular obstacles simulating urban blocks that covered the entire working section, in order to avoid the development of an internal boundary layer due to roughness changes (Sect. 3.1). This experimental set-up, shown in Fig. 1, allowed us to reproduce a boundary layer whose depth δ was approximately 0.8 m.

The obstacles were squares of side 250 mm in plan and 50 mm high, representing 20-m high buildings at the 1:400 scale. The obstacles were aligned and densely packed to model a simplified urban neighbourhood and 14 staggered nuts of 5 mm height were placed over each obstacle to simulate smaller scale roughness elements, such as roofs and chimneys,

Fig. 1 Wind-tunnel experimental set-up and source position

characterising the urban geometry (Salizzoni et al. 2008). The ratio between the obstacle height H and the depth of the boundary layer δ was 1/16 and ensured that a realistic ratio was preserved. Assuming a typical building height of 20 m, this would correspond to a boundary-layer thickness of 320 m. Even if the value of δ would correspond to a quite shallow adiabatic atmospheric boundary layer, it ensures flow dynamics characterised by length scales that are an order of magnitude larger than H, the length scale imposed by the obstacles close to the ground. The reference free-stream velocity U_∞ at the boundary-layer height was set at 5 m s^{-1}. The Reynolds number $Re = U_\infty \delta/\nu \simeq 2.6 \times 10^5$ and the roughness Reynolds number $Re_r = u_* z_0/\nu \simeq 12$ are sufficiently high to ensure the adequate simulation of a fully rough turbulent flow and therefore the dynamical similarity with a flow at full-scale urban geometry. Snyder (1981) stated that $Re_r \geq 2.5$ is required for such a simulation. The obstacle Reynolds number, based on the obstacle height and the free-stream velocity at that height, was $Re_H = U_H H/\nu \simeq 6700$. According to the criterion proposed by Snyder (1992), i.e. $Re_H \geq 4000$, this value ensures the dynamical similarity of the flow around an obstacle immersed in a simulated atmospheric boundary layer.

Dispersion phenomena within and above the array have been studied for different obstacle configurations and wind directions. As Fig. 2 shows, different configurations have been obtained by varying the distances between the obstacles. We varied both S_x, the spacing between the obstacles in the streamwise (x) direction, and S_y, the spacing in the spanwise (y) direction. The wind direction was varied by rotating a section of the obstacle array, as shown in Fig. 1: the upwind edge of the rotated section was at a distance of about 7δ from the beginning of the test section and the geometry of the upwind array was kept unaltered. As specified in Sect. 3.1, due to experimental difficulties, we could not achieve a perfect alignment between the x-axis and the external wind direction. Therefore, we define θ as the angle between the direction of the incident wind and the x-axis of the array (Fig. 2). It is worth noting that the angle θ is a spatially-averaged quantity, calculated from velocity measurements performed over the section of interest of the obstacle array.

The values of S_x, S_y and θ for the different configurations studied are summarised in Table 1, together with the values of the porosity factors λ_P and λ_F, calculated according to the definition given by Grimmond and Oke (1999). Note that Configuration 2 corresponds to Configuration 3 rotated by 90° and that their values of λ_P and λ_F are equal.

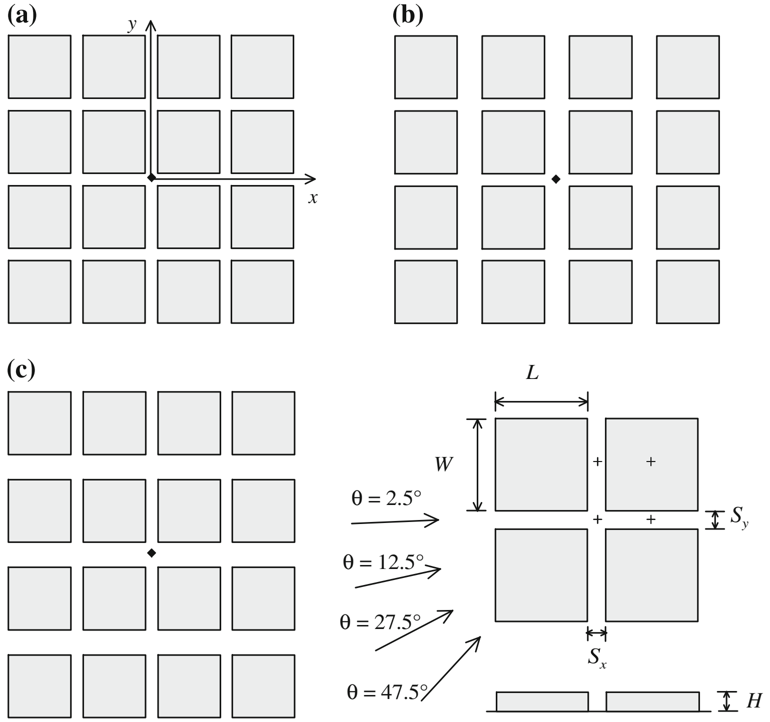

Fig. 2 Diagram of the array set up, including the source release position (*filled diamond*). **a** Configuration 1: $S_y = S_x = H$; **b** Configuration 3: $S_x = 2H S_y = H$; **c** Configuration 2: $S_x = H S_y = 2H$. The *cross* indicate the different positions where the vertical profiles were recorded

Table 1 Geometrical properties of the array and incident wind direction for the different configurations studied

Configuration	S_x/H	S_y/H	λ_P	$\lambda_F(0°)$	θ
1	1	1	0.69	0.14	2.5°, 12.5°, 27.5°, 47.5°
2	1	2	0.59	0.12	2.5°, 47.5°
3	2	1	0.59	0.12	2.5°, 47.5°

See Fig. 2 for the definitions of S_x, S_y and θ; see text for the definition of λ_P and λ_F

The flow dynamics above the obstacle array were investigated by measuring vertical profiles of mean and fluctuating wind velocities with hot-wire anemometry, using an X-wire probe with an acceptance angle of 45° and a sampling frequency of 5,000 Hz.

The pollutant source was placed at height $H/2$ within an intersection located in the middle of the model at a distance of about 10δ from the beginning of the test section. Ethane (C_2H_6) was used as the passive tracer in the experiments because it is neutrally buoyant in air and concentrations were measured by a flame ionization detector (FID). The low flow rate employed in the experiments ensured that the gas was quickly diluted and that passive diffusion started near the source. Calibration was performed by subjecting the FID probe to a series of known and controlled concentrations over an appreciable range. For each measurement point a 120 s time series was acquired, sampled at a frequency of 300 Hz. This averaging time ensures reliable statistics since it is much longer than the typical time scale of the large vortical structures within the boundary layer, which can be roughly estimated as $\delta/u_* \approx 3$ s, where u_* is the friction velocity (Sect. 3.1). The uncertainty of the results was evaluated by collecting repeated runs at the same sampling position. It was found that the near-field mean concentration values are subjected to uncertainties of the order of 3–5%, while for the far-field concentration values the error is higher and can reach 10%.

3 Flow Field

The flow within and above a group of obstacles is characterised by complex flow patterns and extremely complex momentum transfer mechanisms due to non-linear interactions between the eddies generated in the wake of each obstacle. The complexity of the velocity field in a group of obstacles can be further increased by inhomogeneous conditions in the external flow that drives the air motion within the array. This occurs when the inflow wind profile reaches the obstacle array, since a certain fetch is required for the flow to reach a new equilibrium condition (Antonia and Luxton 1971; Belcher et al. 2003). To avoid a further degree of complexity induced by a roughness change, we placed the obstacles over the entire floor of the wind tunnel (Fig. 2) that allowed us to minimise the external flow inhomogeneities in the streamwise direction. In this way we could simulate flow conditions similar to those occurring in infinitely wide arrays, such as those numerically simulated in previous studies (Coceal et al. 2006; Garbero et al. 2011). We therefore expect to observe different flow behaviours and dispersion conditions compared to those observed in arrays of finite size, such as those studied for example by Princevac et al. (2009) and Buccolieri et al. (2010).

In the following, we outline the main characteristics of the velocity field above (Sect. 3.1) and within (Sect. 3.2) the obstacle array for varying street aspect ratio and incident wind direction.

3.1 External Velocity Field

To characterise the dynamics of the external velocity field we recorded vertical velocity profiles over a cross-section of the street network at different positions with respect to the canopy: at the centres of intersection, longitudinal street, transverse street and obstacle, as indicated by the cross in Fig. 2. The profiles were recorded starting from a distance of 9.5δ downstream of the beginning of the test section. At this distance we assume that the development of coherent structures in the wake of the vortex generators has already reached an equilibrium condition and the dynamics of the flow depend only on the scales imposed at the wall and the boundary-layer depth (Salizzoni et al. 2008). From these measurements we inferred both the direction and the vertical structure of the external flow for the different studied configurations.

In this section, we initially present the characteristics of the flow developing over the obstacle array in Configuration 1, then we discuss how different obstacle configurations modify the external flow conditions compared to Configuration 1, and finally we focus on the evaluation of θ, the angle that the external flow forms with the x axis.

Figure 3a and b show the vertical profiles of the streamwise mean velocity and turbulence intensity for Configuration 1 measured at different streamwise distances from the entrance to the wind tunnel. It is evident that the profiles do not differ significantly from one another indicating that the boundary layer has reached an equilibrium condition.

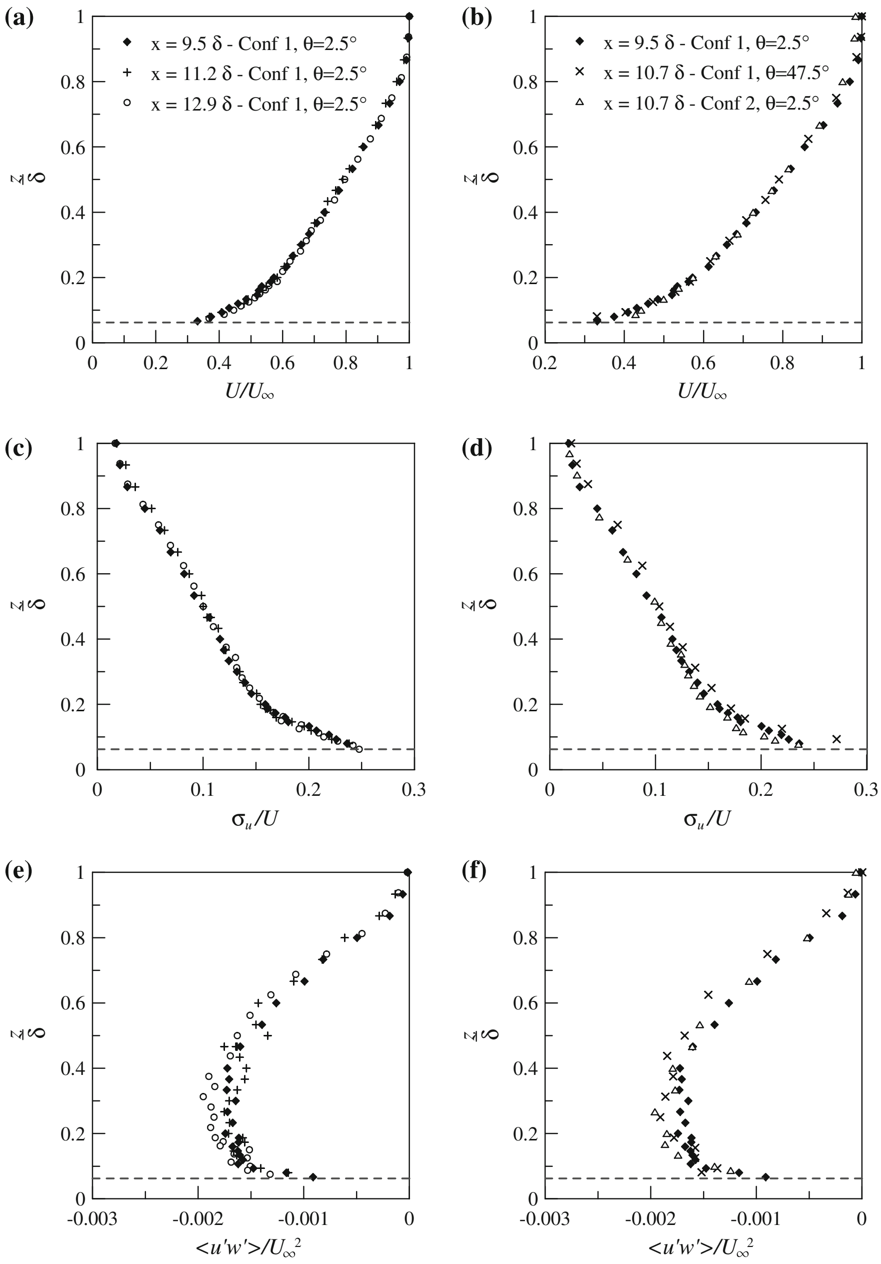

Fig. 3 Boundary-layer evolution along the streamwise direction. Distances are given from the entrance of the wind tunnel. *Dashed line* indicates the obstacle height

The structure of the flow can then be described according to similarity theory (Tennekes and Lumley 1972). This theory assumes that the turbulent velocity field can be divided into different regions and that the flow in each region can be described by some form of similarity solution if appropriate length and velocity scales are chosen. Given this decomposition, the

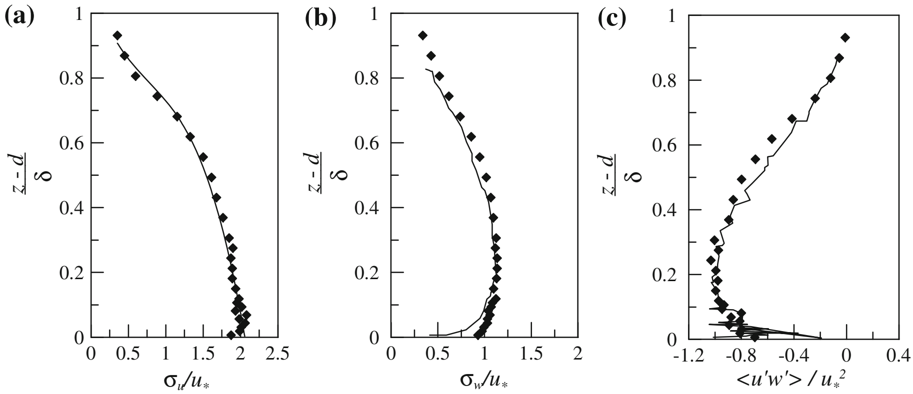

Fig. 4 Normalised velocity profiles for the external flow. *Diamonds*: experimental data from this study; *solid lines*: experimental data from Raupach et al. (1991)

lower part of the boundary layer over a rough wall, the so called ‘surface layer’, is then expected to be composed of two parts: the inertial sublayer, where the flow variables depend on the vertical coordinate only, and the roughness sublayer, where the flow is not homogeneous in the horizontal plane since it is directly influenced by the wakes of individual roughness elements. In the inertial sublayer the mean velocity profile in neutral conditions is usually described by the logarithmic law:

$$\frac{U(z)}{u_*} = \frac{1}{k} \ln\left(\frac{z-d}{z_0}\right) \tag{1}$$

where z_0 is the aerodynamic roughness and d is the zero-plane displacement. In the literature several techniques have been developed to determine the values of these parameters. The method adopted here is that presented by Salizzoni et al. (2008). The value of $u_* = \sqrt{-\overline{u'w'}}$ was inferred from the measured Reynolds stress profile in the lower part of the flow field (Raupach et al. 2006), where u_* attains an almost constant value. As shown in Fig. 3e and f, this occurs in the range $0.14 \le z/\delta \le 0.35$. The other two parameters, z_0 and d, are then estimated through a best fit of the mean velocity profile with the logarithmic law (Eq. 1). Since the logarithmic profile only applies to a fraction of the full velocity profile, it is necessary to limit the fitting procedure to a subset of the measured profiles. The upper and lower limits for the subrange are the same adopted to compute the friction velocity u_*.

The computed values of u_*, z_0 and d are given in Table 2, together with the uncertainties associated with their estimation; these were obtained from stochastic simulations of the data, using the known errors for U, u_* and z (Salizzoni et al. 2008). The values for z_0 and d are in agreement with previous results for flows over two-dimensional obstacles in the skimming flow regime (Salizzoni et al. 2008). These show that, when the obstacles are sufficiently packed together, the zero-plane displacement turns out to be equal to the obstacle height and the wall roughness is between two and three order of magnitude smaller that the obstacle size. The vertical profiles of the Reynolds stress $-\overline{u'w'}$ and the root-mean-square (r.m.s.) of the velocity components σ_u and σ_w are shown in Fig. 4a–c. The flow variables are presented in normalised form and are compared to the experimental data of a previous study (Raupach et al. 1991): the curves obtained from the two datasets show good agreement. We infer that the profiles of each flow variable normalised on u_* collapse onto a single curve that is an

Table 2 Boundary-layer parameters

u_*/U_∞	$0.046 \quad \pm 0.002$
d/δ	0.0625 ± 0.003
z_0/δ	0.0011 ± 0.0001

The values are representative of all configurations studied (see text)

invariant function of the normalised vertical coordinate $\eta = (z-d)/\delta$, as stated by similarity theory (Tennekes and Lumley 1972). It is worth noting that the scaling of the profiles agrees well with that predicted by the theory even though the ratio $\delta/z_0 \simeq 930$ is quite far from the asymptotic condition required.

Velocity profiles measured at different streamwise positions for other studied configurations are compared with the respective profiles for Configuration 1. The results indicate that the mean velocity profiles vary only very slightly for different incident wind directions and for different geometrical layouts, as shown in Fig. 3c. Some differences can be detected in the vertical profiles of the turbulence intensity. As shown in Fig. 3d, these differences are concentrated in the lowest part of the boundary layer, close to the top of the obstacles, in the roughness sublayer.

The upper limit of the roughness sublayer, which we refer here to as the ‘blending height’ z_*, is defined as the limit where horizontal inhomogeneities remain below an arbitrary threshold value. Note that the definition of blending height adopted here for a homogeneous surface differs from that given in the case of heterogenous surfaces (Goode and Belcher 1999), who defined the blending height as the top of the highest extent of the internal boundary layer. We inferred z_* by quantifying the horizontal inhomogeneity of the velocity field from the vertical profiles of different flow variables at different positions above the canopy. Our results indicate that for Configurations 1 and 2 ($\theta = 2.5°$) the depth of the roughness sublayer is almost negligible ($z_* \simeq H$) and increases with increasing incident wind direction, reaching a maximum at $\theta = 47.5°$. Conversely, in Configuration 3, the depth of the roughness sublayer is almost the same both for $\theta = 2.5°$ and $\theta = 47.5°$ and extends to a height of about $2H$ from the ground. A detailed investigation of the dynamics of the roughness sublayer is beyond the scope of this work. Here we only show that the turbulence intensity within it has similar values for $\theta = 2.5°$ in Configuration 1 and 2 and increases for an increasing angle of the incident wind $\theta = 47.5°$ (Fig. 3d).

Even though the depth of the roughness sublayer varies from one configuration to another, it is worth noting that, in the remainder of the external boundary layer, the flow is almost insensitive to the different geometrical layouts and to the incident wind direction, as is clearly shown by all profiles presented in Fig. 3a–f. We can assume therefore that the values presented in Table 2 are representative of all configurations studied. This result can be explained by the fact that the drag on the overlying flow is mainly exerted by the nuts placed on the top of the obstacles rather than the obstacles themselves. As shown by Salizzoni et al. (2008), this happens in particular conditions in the skimming flow regime, when the obstacles are sufficiently densely packed.

From the measurements of the two components of the mean horizontal velocity at $z = 3H$, which occurs above the blending height for all the configurations, we have evaluated the local wind direction $\theta_i(x, y)$. We used $\theta_i(x, y)$ to compute the spatial average and standard deviation, referred to as θ and σ_θ respectively. The spatial variability of θ, defined as σ_θ, was approximately the same for all configurations and equal to $\pm 2.5°$. We highlight this because, with inherent experimental difficulties, a parallel wind direction $\theta = 0°$ was unachievable

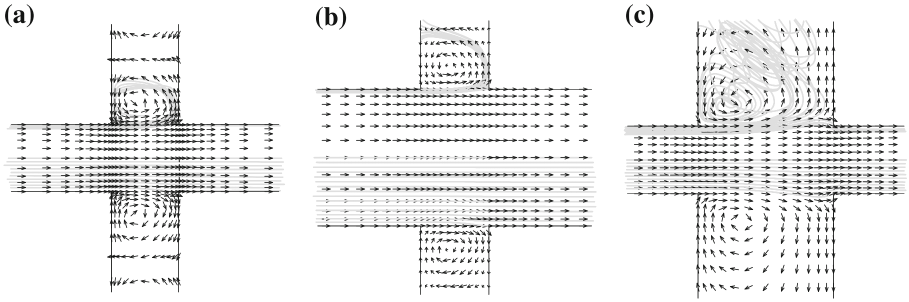

Fig. 5 Mean flow streamlines and mean velocity field in Configuration 1 (**a**), Configuration 2 (**b**) and Configuration 3 (**c**). Numerical simulations for $\theta = 0°$ by Garbero et al. (2011)

in our experiment. When the obstacle array was perfectly aligned with the wind-tunnel axis, we measured a wind direction of $\theta = 2.5°$.

3.2 Flow Within the Obstacle Array

The aim here is not to give a detailed description of the velocity field within the obstacle array, as performed for instance by Coceal et al. (2006) or Santiago and Martilli (2007), but to point out the characteristics of the flow that is useful for interpreting passive scalar concentration measurements. To this end we summarise the main results, both numerical and experimental, obtained in previous works (Soulhac et al. 2008, 2009; Garbero et al. 2011).

3.2.1 Influence of the Geometrical Layout

The numerical and experimental results presented by Soulhac et al. (2009) focus on the influence of a street intersection on the flow within a street compared to that observed in the case of a two-dimensional street canyon with an external wind perpendicular to the street axis. They show that the intersection modifies the classical recirculating flow within the street and that a vortex with a vertical axis is set up close to the edges of the street inducing a complicated 3-D structure in the mean flow. For an aspect ratio $H/S_x = 1$ the transverse dimension of this vortex extends to $1.4S_x$ and $2.2S_x$. However, the influence of the intersection on the flow in the crossing street depends on the aspect ratio of the street forming the intersection.

Numerically computed mean flow streamlines presented by Garbero et al. (2011) provide further evidence of the flow patterns that characterise the mean velocity field for the three different array configurations (Fig. 5). The flow patterns in Configurations 1 and 2 are very similar: a vertical axis vortex close to the intersection is driven by the flow within the intersection and interacts with the horizontal axis vortex, which in turn is driven by the external flow. The resulting vortex evolves along the street and when the perturbations due to the presence of the intersection weaken, it becomes an across-street recirculation vortex. In these conditions the mean velocity streamlines in the parallel street only weakly interact with those in the perpendicular streets. Therefore, the flow within the streets in these configurations is almost decoupled from that developing in the crossing streets and from the external flow. This indicates a general decoupling of the flow that reduces the interaction between the external and recirculating flows. Conversely, the structure of the flow within the street in Configuration 3, i.e. $S_x = 2H$, appears radically different: the recirculating cell with a vertical axis located close to the intersection is confined to the upwind corner and does not occupy the whole section of the crossing street. In this case a strong interaction between the flows within the street and the intersection is observed. The streamlines originating in the external flow penetrate into the cavity and a complex vortical structure occurs within the street.

These results show that, for $\theta = 0°$, the key parameter that determines the structure of the flow is S_x/H, namely the aspect ratio of the street perpendicular to the wind direction. This parameter fixes both the size of the interface between the street and the intersection and the size of the interface between the street and the external flow.

3.2.2 Influence of the Incident Wind Direction

The flow field in a street canyon for any wind direction is characterised by a helicoidal motion due to the superposition of an across-street recirculation vortex and an along-street channelling (Dobre et al. 2005; Soulhac et al. 2008, 2009). Assuming the theoretical model proposed by Soulhac et al. (2008), the component of the spatially-averaged velocity along the street axis, referred to as U_{street}, can be computed from:

$$U_{\text{street}}(\theta) = U_{\text{street}}(\theta = 0°)\ \cos\theta \tag{2}$$

where θ is the external wind direction. This model, which has been tested by comparison with numerical simulations, was developed for the case of an infinitely long street. However, the presence of intersections at the street edges induces modifications in the flow field within the street compared to that within an infinitely long street. A quantitative estimate of the influence of the intersection on the flow within the street was presented by Soulhac et al. (2009), who calculated the spatially-averaged velocity within it by means of numerical simulations. Here we present a further estimate, computed by exploiting the experimental data available from Garbero (2008) that includes measurements of the mean velocity component parallel to the street axis, U_{street}, along the street axis itself. The measurements were performed at M different points (y_i, $x = 0$, $z = H/2$). We hence obtain an estimate for the spatially-averaged velocity by calculating:

$$U_{\text{street}} \simeq \frac{1}{M}\sum_{i=1}^{M} U_{\text{par}}(y_i, x = 0, z = H/2). \tag{3}$$

In Fig. 6a we compare the values both estimated by Eq. 3 and computed numerically by Soulhac et al. (2009) for a street of finite length to the theoretical values given by Eq. 2 for a street of infinite length but identical aspect ratio. We observe some differences between the estimates obtained by experimental and numerical data, especially for orientations $\theta = 12.5°$ and $\theta = 47.5°$. Since the experimental value represents a quite rough estimate, whose reliability should be verified by means of more detailed velocity measurements, we can not give an accurate interpretation of these differences. However, both numerical and experimental data show that the mean velocity through a street of finite length is reduced and is not proportional to the longitudinal projection of the external wind. This clearly points out the influence of the intersection on the flow within the adjacent streets. Compared to the case of an infinite street, some fraction of the kinetic energy of the mean flow is transferred to the vortical structures originating close to the intersections and then dissipated by smaller scale vortices, thus reducing the spatially-averaged velocity within the street.

From these data we may also evaluate the spatially-averaged direction of the flow within the canopy, which is fixed by the spatially-averaged velocity in two perpendicular streets. Using the data plotted in Fig. 6a, this can be computed from

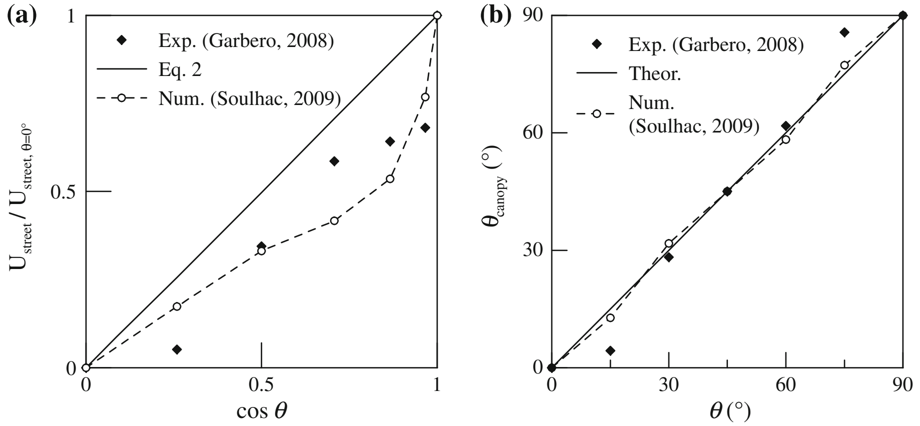

Fig. 6 **a** Spatially-averaged velocity within a street, and **b** direction of the mean velocity within the canopy as a function of the external wind direction θ: comparison between the experimental and numerical values and the theoretical model proposed by Soulhac et al. (2008)

$$\theta_{\text{canopy}} = \arctan\left\{\frac{U_{\text{street}}(\pi/2-\theta)}{U_{\text{street}}(\theta)}\right\}. \tag{4}$$

Numerical and experimental estimates of θ_{canopy} are compared to those predicted by Eq. 2 in Fig. 6b. The numerical results indicate that θ_{canopy} does not differ significantly from that given by Eq. 2, which corresponds to the direction θ of the external wind, even if the numerical estimates of U_{street} are considerably different from those given by Eq. 2. Numerical and experimental results do not differ significantly from each other for $30° < \theta < 60°$, whereas we observe significant differences for $\theta = 15°$ and $\theta = 75°$. This suggests that for $0° < \theta < 30°$ (and $60° < \theta < 90°$) the values of θ_{canopy} may be significantly smaller than θ. However the lack of data in this region precludes a precise definition of the dependence of θ_{canopy} on θ for these angles; for that purpose we need a more detailed experimental characterisation of the flow dynamics within the street. Some additional information will be inferred indirectly from the analysis of the passive scalar concentration results presented in the following section.

4 Pollutant Dispersion

In order to point out the principal processes that determine the dispersion of a passive scalar within a street network, we have studied the spatial evolution of a plume due to a steady release of pollutant from a ground-level source, placed at a street intersection, at a height of $H/2$ and at a distance of approximately 10δ from the vortex generators. We recorded horizontal and vertical profiles of mean concentration at different distances downwind of the source between $x = 6H$ and $x = 40H$ from it. In order to analyse the different profiles, the mean concentrations are expressed in a standard dimensionless form:

$$K(x, y, z) = \frac{C U_H L H}{Q} \times 10^{-6} \tag{5a}$$

where C is the measured mean concentration in ppm, Q is the emission rate in m^3s^{-1}, H is the height of the obstacles, $L (= 5H)$ is their length, and U_H is the velocity at height H. From the values of $K(x, y, z)$ we define the following quantity:

$$K_0(x, z) = \max_{y \in]-\infty, +\infty[} \{K(x, y, z)\}\,. \tag{5b}$$

The moments of the measured concentration distributions $K(y)$ and $K(z)$ have been calculated in order to describe the overall plume behaviour, and are defined as follows:

$$y_c = \frac{\int_{-\infty}^{+\infty} y\, K(y) dy}{\int_{-\infty}^{+\infty} K(y) dy}, \tag{6}$$

$$\sigma_y^2 = \frac{\int_{-\infty}^{+\infty} (y - y_c)^2 K(y) dy}{\int_{-\infty}^{+\infty} K(y) dy}, \tag{7}$$

$$\sigma_z^2 = \frac{\int_{0}^{+\infty} z^2 K(z) dz}{\int_{0}^{+\infty} K(z) dz}\,. \tag{8}$$

The zero central moment defines the plume centreline y_c, while the standard deviations identify the lateral and vertical dispersion parameters σ_y and σ_z. Since data exist only for $z > 0$, the moments of the vertical distribution are calculated as if the distribution were symmetric with respect to the ground.

In the following, the normalised concentration $K(y)/K_0$ is plotted as a function of $(y - y_c)/\sigma_y$ and compared to the normal Gaussian curve of parameters $y_c = 1$ and $\sigma_y = 1$. This approach is in contrast to that of other authors (Davidson et al. 1996; MacDonald et al. 1998), who fitted the measured profiles to Gaussian curves in order to derive these parameters.

Some preliminary experiments were performed for the dispersion from the ground-level source by removing the obstacles downwind of the source and leaving the upwind array unchanged. We refer to this configuration as *open terrain*, even if the flow field downwind of the source shows similarities with that downwind of a backward facing step (Sect. 4.1.3). The transverse profiles measured at heights $z = H/2$ and $z = 2H$ and distances downwind of the source $x = 21H$ and $x = 35H$, and the vertical profile measured at $x = 35H$ and $y = 0$, are fitted by the normal Gaussian curve with a correlation coefficient $R^2 = 0.99$. Since the vertical distribution is assumed to be symmetric with respect to the ground, the image source is placed at $z = 0$ and the usual reflected Gaussian fitting the vertical profile becomes a simple Gaussian curve. The experimental data show that the spatial distribution of the mean concentration can be fairly well approximated by a Gaussian curve even in a highly sheared mean flow with anisotropic turbulence (Fackrell and Robins 1982). The lateral and vertical spreading of the plume in open terrain will be used in the following section as a reference to evaluate the overall plume spreading within the obstacle array.

4.1 Influence of the Geometrical Layout

In order to study the effect of the geometrical layout on the dispersion pattern, we have investigated the evolution of the plume in the three different array configurations for a wind direction of $\theta = 2.5 \pm 2.5°$ (Sect. 3.2).

4.1.1 Configuration 1 and 2

The horizontal profiles of mean concentration measured both within and above the array for *Configuration 1* and the associated plume spreading are presented in Fig. 7. Within the array the plume is mainly confined to the street within which the source is located (Fig. 7a). This is what we refer to as the ‘channelling’ of the plume, a mass transfer process that is dominated by the mean advective fluxes along the axis of one street and which implies reduced fluxes in the transverse direction. To explain this phenomenon we turn to the numerical results discussed in Sect. 3.2.1, obtained for slightly different conditions of the external wind, i.e. $\theta = 0°$ instead of $\theta = 2.5°$. These results show that, for low incident angles, the mean volume flux across the street-intersection interfaces is almost zero and the turbulent diffusion is the principal contributor to the mass transfer into the crossing street. Similarly, there are almost no mean advective pollutant fluxes along the perpendicular streets and the mass transfer along their axes is only due to a diffusive transfer, which explains the sharp concentration gradients observed there. The channelling of the plume results in a reduced spreading within the array compared to that observed in the overlying flow. By fitting to a straight line the values of the plume centreline y_c calculated within and above the array, we determined the overall direction of the plume θ_c within and above the array. The value of θ_c within the array is very close to zero, i.e. the plume centreline is parallel to the axis of the street within which the pollutant is emitted, while it is higher above the array, $\theta_c = 1.2°$, even if smaller than $\theta = 2.5°$, the external wind direction. It is worth noting that the values of the plume deflection for small incident angles may be affected by the non-negligible relative errors related to the wind-tunnel set-up.

Figure 7b shows that the profiles are self-similar both within and above the array, but the shape of the curves is significantly different in the two regions. The profiles above the array are well fitted by the Gaussian curve. Figure 7c shows the vertical profiles of the mean concentration for different downwind positions; the vertical profiles have a relatively large vertical gradient from ground level up to $z/H \simeq 3$ even at large distances from the source. This suggests that the diffusivity in the lower part of the external flow is reduced approaching the top of the obstacle just as in a flow over flat terrain. In such a flow the diffusivity decreases approaching the ground as the integral length scale is progressively reduced. We can therefore infer that the obstacles and their size and spacing have little influence on the dispersion process in the overlying boundary-layer flow. We discuss this feature further in Sect. 4.1.3.

Figure 8 shows the behaviour of the plume in *Configuration 2*. The horizontal profiles in Fig. 8a show evidence of the channelling of the plume that constrains its lateral spreading within the array. The near-field behaviour of the plume is quite different to that in Configuration 1, since at $x = 6H$ (which corresponds to the first intersection), a sharp cut occurs in the concentration profile at the interface between the intersection and the lateral street, at $y = \pm H$. Here, the concentration distribution is narrower than that observed at the same position in Configuration 1. These features suggest that the channelling is even more effective than in the previous case. This is confirmed by the fact that the lateral plume spreading within the array is reduced not only with respect to that in the external flow but also to the corresponding values for Configuration 1. Furthermore, the values of θ_c correspond to the direction of the street within which the pollutant is emitted and are very similar to those in Configuration 1, i.e. $\theta_c = 0.4°$ within the array and $\theta_c = 1.2°$ above it.

As shown in Fig. 8b, the normalised concentration profiles within the array show less scatter than those in Configuration 1 and approach more closely the self-similar curves characterising the external profiles at $z = 2H$. Figure 8c shows the vertical profiles of the

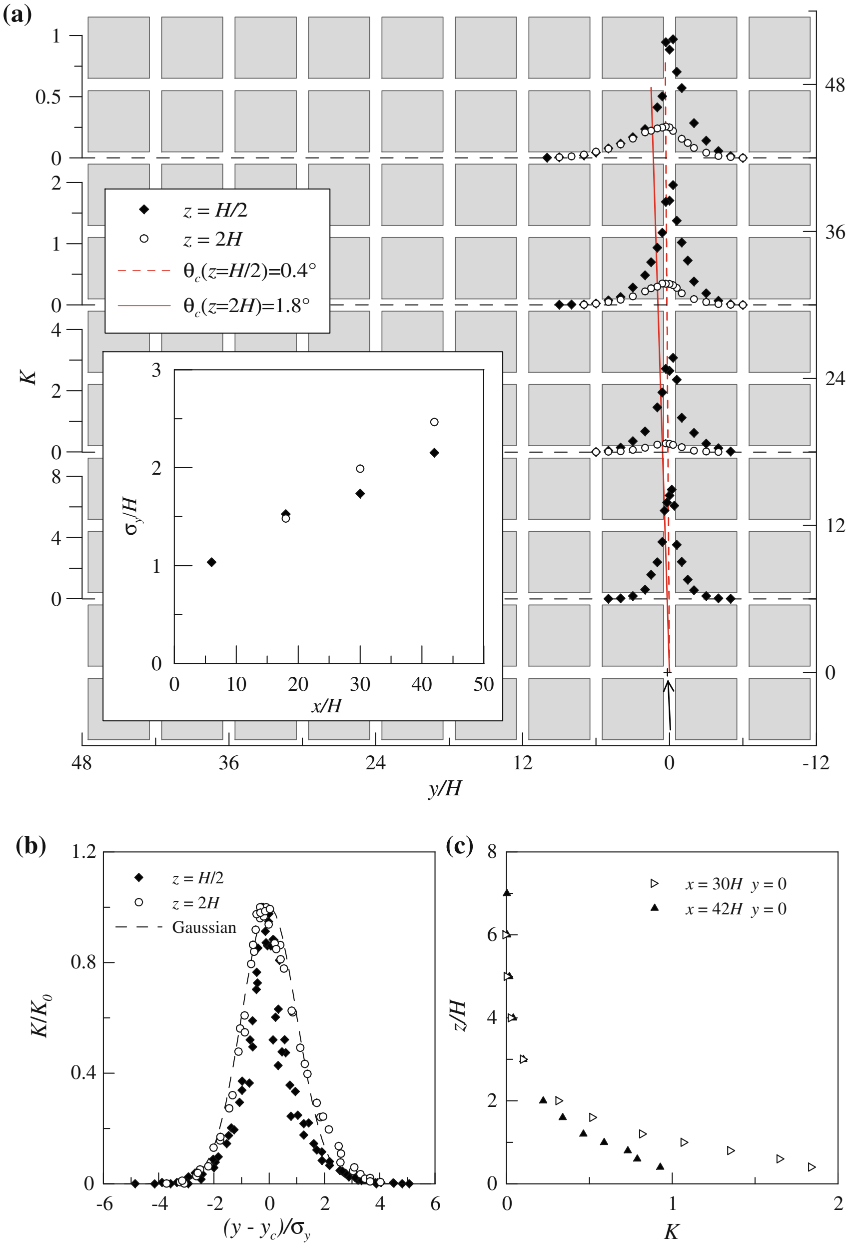

Fig. 7 Plume behaviour throughout the array for $\theta = 2.5°$, *Configuration* 1. **a** Horizontal mean concentration profiles at various positions downwind of the source (+) within and above the array. In the window, the spatial evolution of the horizontal plume spreading is shown. **b** Normalised horizontal mean concentration profiles compared to the unitarian Gaussian, and **c** vertical mean concentration profiles at various positions downstream the source

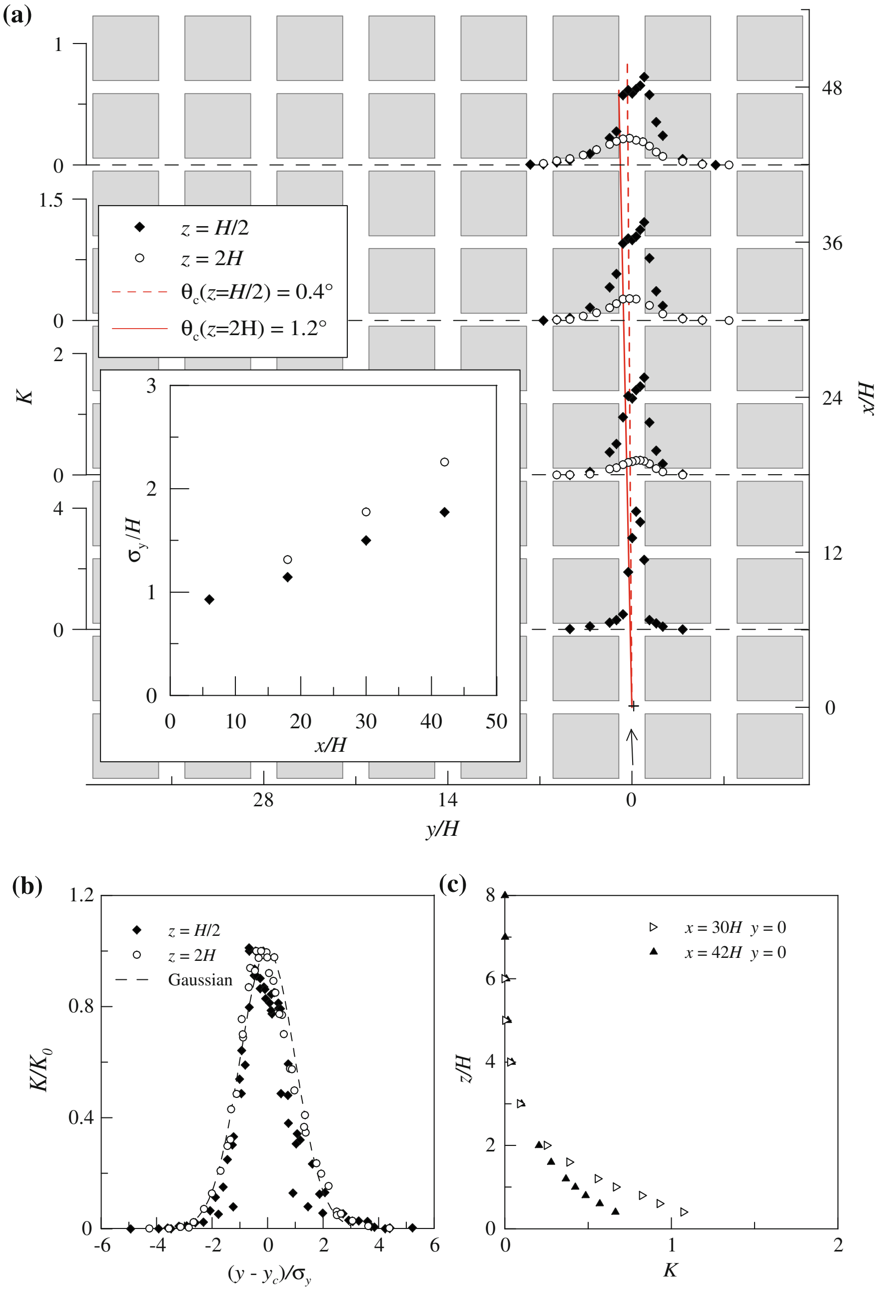

Fig. 8 Plume behaviour throughout the array for $\theta = 2.5°$, *Configuration* 2. **a** Horizontal mean concentration profiles at various positions downwind of the source (+) within and above the array. In the window, the spatial evolution of the horizontal plume spreading is shown. **b** Normalised horizontal mean concentration profiles compared to the unitarian Gaussian, and **c** vertical mean concentration profiles at various positions downstream the source

mean concentration for different downwind positions, which are very similar to those in Configuration 2.

4.1.2 Configuration 3

The behaviour of the plume throughout the array for *Configuration 3* is shown in Fig. 9. The horizontal profiles plotted in Fig. 9a are significantly different from those for the two previous configurations. The profiles within and above the array are more similar to each other and in the far-field ($x/H = 35$) the profile within the array matches that above. This difference can be partially explained by the numerical results presented in Fig. 5: compared to the previous configurations, the larger lateral streets induce a more complex streamline topology that causes a less effective channelling of the flow in the longitudinal streets and therefore an enhanced mass transfer in the transverse direction. As a result, the normalised horizontal mean concentration within the array fits quite well to a Gaussian curve, as happens for those above the array (Fig. 9b). However, the topology of the velocity field analysed in Sect. 3.2.1 for the case $\theta = 0°$ does not allow us to explain the important deflection of the plume centreline from the x axis observed in Fig. 9a. The value of θ_c is approximately 7° within the array and 5.8° above it, significantly exceeding the external wind deflection of 2.5°. This feature suggests that the flow within the array is extremely sensitive to slight geometrical asymmetries. The effect of these asymmetries is amplified by the instabilities arising in highly sheared flow at street intersections and gives rise to dispersion patterns that are not easily predictable from velocity measurements in the external flow. This happens when the non-dimensional width of the crossing street S_x/H is increased and the instabilities generated in the shear layers at street intersections have sufficient time to grow and interact nonlinearly with the larger scale vertical axis vortex located at the corners of the crossing street (Fig. 5). The same effect was observed by Hoydysh and Dabberdt (1994) in an idealised street intersection. By means of flow visualization they showed that a slight deflection of the external wind direction could be amplified by small geometrical irregularities of the array and induce a high asymmetry to the spatial evolution of the plume.

In Fig. 9c we show the vertical concentration profiles recorded at increasing distances from the source along the x-axis. The shape of the profiles differs significantly from that observed in Configurations 1 and 2, since they show almost constant concentration values close to the top of the obstacles. These reduced concentration gradients are related to the enhanced vertical diffusion that characterizes the roughness sublayer compared to that in the inertial sublayer (Raupach et al. 1980; Salizzoni et al. 2009b). As shown by Salizzoni et al. (2009b), the comparatively higher diffusivity in the roughness sublayer can be explained by an incremented integral length scale within it, whose size approaches that of the obstacle height.

4.1.3 Comparative Discussion

Figure 10 compares the spatial evolution of the dispersion parameters σ_y and σ_z in the three array configurations and in open terrain.

The horizontal plume spreading σ_y in Configurations 1 and 2 is reduced compared with those in open terrain, whereas a slight enhancement is observed for Configuration 3. This behaviour differs from the enhanced spread found in other studies (Davidson et al. 1996; MacDonald et al. 1997) for blocks with the same spacing, $S_x/H = 1$, but different lateral dimension, $L/W = 1$. The larger lateral dimension of the buildings therefore plays a major

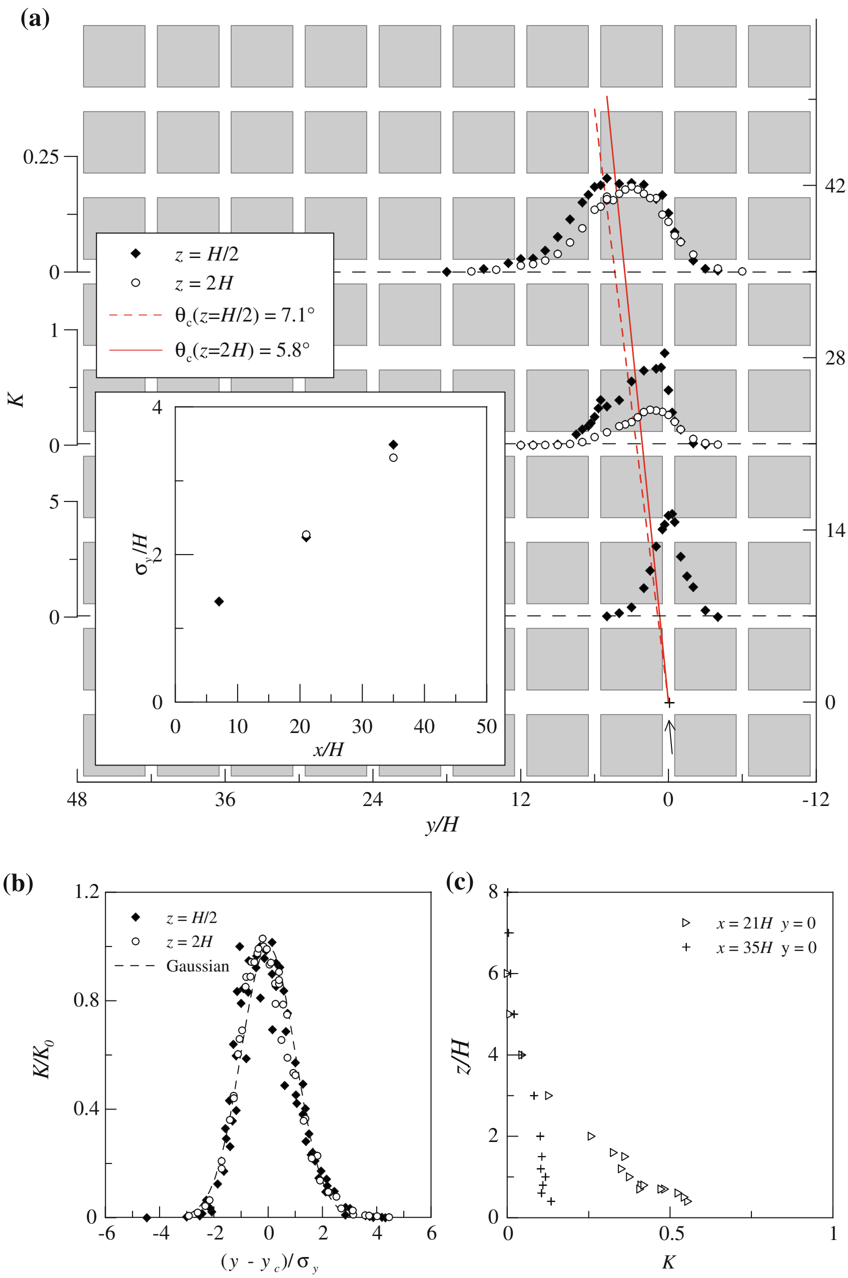

Fig. 9 Plume behaviour throughout the array for $\theta = 2.5°$, *Configuration* 3. **a** Horizontal mean concentration profiles at various positions downwind of the source (+) within and above the array. In the window, the spatial evolution of the horizontal plume spreading is shown. **b** Normalised horizontal mean concentration profiles compared to the unitarian Gaussian, and **c** vertical mean concentration profiles at various positions downstream the source

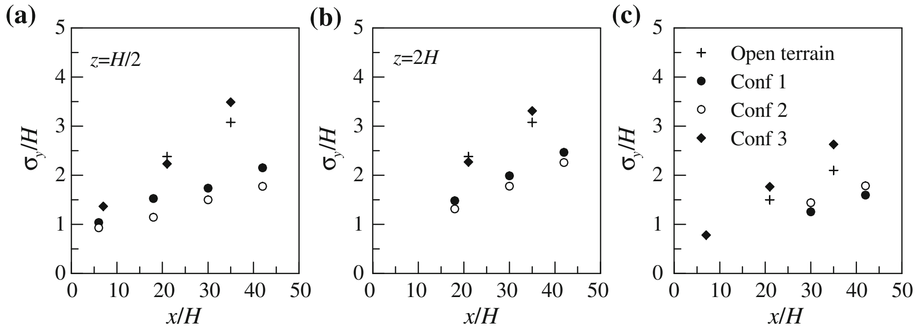

Fig. 10 **a**–**b** Lateral plume spreading within and above the array, and **c** vertical plume spreading as a function of distance from the source in the different studied configurations for $\theta = 0°$

role in inhibiting lateral dispersion and the plume spreadings within the array are not necessarily enhanced compared to those observed in open terrain. We stress that this result is strictly related to the regularity of the array and may not be applicable in more realistic configurations made up of equally dense arrays but with significant departures from uniformity, both in height and plan, that would promote lateral and vertical mixing.

The results show that σ_y for Configurations 1 and 2 is very similar and differs significantly from that of Configuration 3 (Fig. 10a). This suggests that for the regular array considered here the parameter S_y/H (which is the same for Configurations 1 and 3, see Table 1) has little influence on the dispersion patterns. Conversely, the horizontal plume spreading is much more sensitive to variations in S_x/H, which fixes both the size of the surface that separates the intersection and the lateral street and the surface that separates the lateral street and the external atmosphere. For $S_x/H = 1$ (Configurations 1 and 2), the plume is channelled in the longitudinal street within which it was emitted and the transfer in the lateral streets is almost completely due to the fluctuating component of the flow (Sect. 3.2.1). For $S_x/H = 2$ (Configuration 3), the channelling is reduced and lateral plume spreading is enhanced. In this case the pollutant transfer at the street intersection is due both to turbulent and mean fluxes, since some of the mean flow streamlines pass from the parallel to the perpendicular street (Fig. 5). Furthermore the dispersion patterns are extremely sensitive to asymmetries in the geometrical layout (Sect. 4.1.2), which give rise to a direction of the plume centreline that can be significantly different from the direction of the external wind (Fig. 9). An enhanced σ_y within the canopy implies also enhanced σ_y values in the external flow, since the plume within the canopy acts as a distributed source for the overlying flow. For this reason σ_y values in the external flow in Configuration 3 are larger than those in Configurations 1 and 2 (Fig. 10b).

The ratio S_x/H appears to be the parameter that shows the greater correlation with the vertical spread σ_z. As shown in Fig. 10c, the values of σ_z in Configurations 1 and 2 ($S_x/H = 1$) are almost the same and are both smaller than those in Configuration 3 ($S_x/H = 2$). This difference is related to the different vertical extension of the roughness sublayer in the configurations. Its extension attains $2H$ in Configuration 3 while it is almost negligible in Configurations 1 and 2. The increased diffusivity within the roughness sublayer in Configuration 3 is then responsible for the larger plume spreading σ_z observed in our experiments. It is worth noting that the values for the case referred to as 'open terrain' are almost the same as those for Configuration 3. The velocity field in the 'open terrain' case shows some similarities with the flow past a backward facing step, as observed in Sect. 4. Therefore the dispersion patterns are determined by the dynamics of vortices whose size is H (Hunt and Castro 1984), as occurs within the roughness sublayer for Configuration 3. This may explain the similar values of σ_z in the two cases.

Comparing the results in Configurations 2 and 3 we conclude that, even if the surface exchanges between the canopy and the external flow are equal,[1] the vertical and horizontal extensions of the pollutant plume above the array are clearly larger in Configuration 3. This means that the vertical exchange velocity of pollutant is more effective in Configuration 3, which has wider perpendicular streets. This feature shows that the vertical exchange is much more effective in the street whose axis is perpendicular to the external wind direction rather than parallel. This is due to the different dynamics of the mixing layer at the top of the streets depending on the external flow direction. Numerical results presented by Soulhac et al. (2008) show that, in a street parallel to the external wind and for aspect ratios $H/W \leq 1/2$, the shear at the top of a street is significantly reduced compared to that observed in the case of the street axis perpendicular to the external wind (Salizzoni 2006; Salizzoni et al. 2009b). Since higher shear implies higher turbulent exchanges, we expect the vertical transfer of momentum and mass to be more effective for streets perpendicular to the external wind.

4.2 Influence of the Wind Direction

The analysis of the results presented in the previous section shows that, in Configurations 2 and 3, identical arrays with different flow orientations result in totally different dispersion patterns. This demonstrates that the role of the obstacles in the dispersion is not only determined by geometrical parameters such as λ_P and λ_F but also depends strongly on the external wind direction. We therefore focussed on the influence of the wind direction on the evolution of the plume within the array for wind directions of 12.5°, 27.5° and 47.5°.

4.2.1 Configuration 1: $\theta = 12.5°$

Figure 11a shows plots of the horizontal profiles of the normalised mean concentration measured within and above the array for $\theta = 12.5 \pm 2.5°$. The direction of the plume centreline θ_c both above and within the array is smaller than the incident angle of the external wind θ. The direction within the canopy is $\theta_c \simeq 5.6°$. We can therefore infer that θ_{canopy}, the spatially-averaged direction of the wind within the canopy, is significantly smaller than θ. This result is in agreement with the experimental estimates of θ_{canopy} presented in Fig. 6b and suggests that θ_{canopy} can be significantly different from θ, even in a regular obstacle array, such as the one investigated here. The curves within the array are asymmetrical and the maximum is located in the same street as the source due to the channelling of the plume, as we observed for $\theta = 2.5°$. The angle of the wind direction with respect to the x-axis produces a mean convective mass flux along the axis of the perpendicular streets, which results in an asymmetrical mass transfer between the streets. Nevertheless, the gradients of the pollutant concentration within the perpendicular streets reveal that the mass transfer is still influenced by a diffusive component and hence the magnitude of the mean convective flux is small. Given these conditions, it is worth noting that the profiles above the array are symmetric with respect to the plume centreline and agree well with the Gaussian model (Fig. 11b), while the enhancement of the plume spreading is slightly greater within the array than above it. The peak concentration recorded in the array has no corresponding

---

[1] Configuration 3 is equivalent to Configuration 2 rotated by 90°.

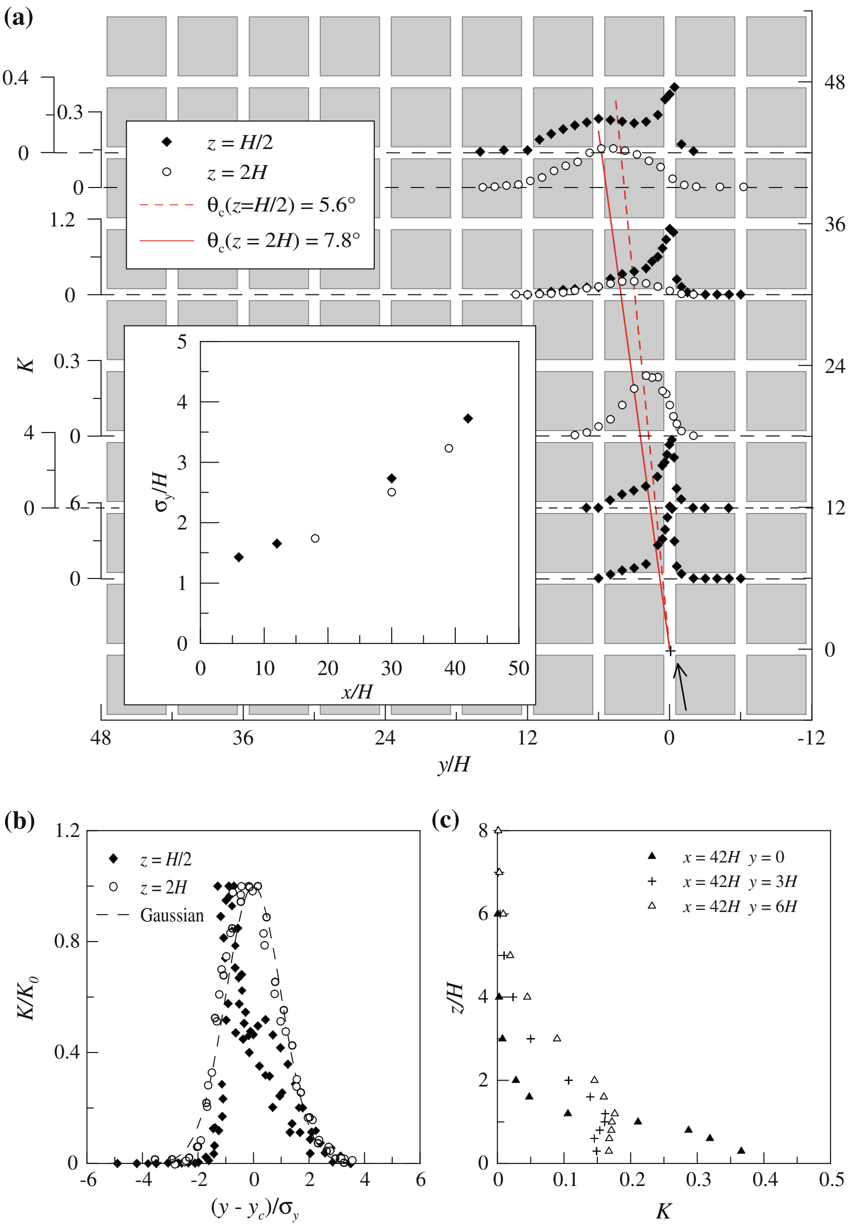

Fig. 11 Plume behaviour throughout the array, $\theta = 12.5°$—*Configuration 1*. **a** Horizontal mean concentration profiles at various positions downwind of the source (+) within and above the array. In the window, the spatial evolution of the horizontal plume spreading is shown. **b** Normalised horizontal mean concentration profiles compared to the unitarian Gaussian, and **c** vertical mean concentration profiles at various positions downstream the source

value in the concentration field above it. We interpret this as further proof that the vertical exchanges between canopy and atmosphere principally take place within the streets whose axis is the most deflected compared to the external wind direction, as discussed in Sect. 4.1.3.

In Fig. 11c the vertical profiles of normalised mean concentration are shown at different positions along the y-axis. We observe that, within the canopy, the maximum concentration occurs within the street where the source is placed, even at large distances from the source ($x/H = 42$). These profiles are very similar to those observed for $\theta = 2.5^\circ$ and show again how weak the vertical turbulent transfer is within a street whose axis is parallel (or nearly parallel) to the external wind direction. In the two other profiles the peak is shifted and is located at about $z = H$, where there is a high concentration gradient. As discussed in Sect. 4.1.1 the presence of these strong concentration gradients close to the top of the obstacles is strictly related to the small vertical extent of the roughness sublayer. It is worth noting that, even at large distances from the source, the concentration field shows significant inhomogeneities, as the vertical concentration gradient at the canopy-atmosphere interface $\partial C/\partial z\ |_{z=H}$, and hence the mass flux, can assume opposite signs over relatively short distances. This is evident in Fig. 11c, which shows that the gradient is positive in the position $x/H = 42$ and $y/H = 0$ and negative in the two other cases.

4.2.2 $\theta = 27.5^\circ$

Figure 12a shows the horizontal profiles of the normalised mean concentration within and above the array for $\theta = 27.5 \pm 2.5^\circ$. The direction of the plume centreline above the array is almost the same as that of the external wind, whereas within the array it is reduced and equal to 21.2°. The channelling mechanism is still evident in the street where the pollutant is released, even though the wind direction is now more inclined compared to the x-axis so that the y component of the velocity within the transverse streets is increased together with the related pollutant mean flux. The presence of these mean convective fluxes along the y-axis of the streets determines a pollutant distribution within the array that is significantly different from that observed for smaller angles. In fact, the mean concentration remains roughly constant throughout the transversal streets with abrupt variations at the intersections, and the horizontal plume spreading σ_y within the array exceeds significantly that above it. Physically this is probably due to very efficient mass transfers in the transverse direction within the array: the mean convective fluxes of pollutant along the y-axis are larger than both the vertical fluxes at the top of the canopy and the ‘diffusive’ fluxes in the y direction within the street. The resulting non-dimensional profiles within the canopy have an irregular shape and cannot be reasonably fitted by any theoretical profile, whereas the profiles above the array are well fitted by a Gaussian (Fig. 12b).

The vertical profiles of the mean concentration shown in Fig. 12c are characterised by very different shapes depending on the sampling positions within the array. It is worth noting that the shape of the profiles is quite irregular close to the ground within the street intersections, and agrees with profiles obtained by previous authors (Hoydysh et al. 1995; Robins et al. 2002; Soulhac et al. 2009) who found the high variability of concentration within the intersection. This is due to the large difference in concentration in the air flow arriving from the different street crossings, as clearly shown in Fig. 12a. For sufficiently large distances from the source the vertical concentration profiles exhibit almost constant concentration values in the lower part of the external flow, close to the top of the obstacles. As for Configuration 3, this is due to the higher diffusivity in the roughness sublayer, whose vertical extent reaches $z = 2H$.

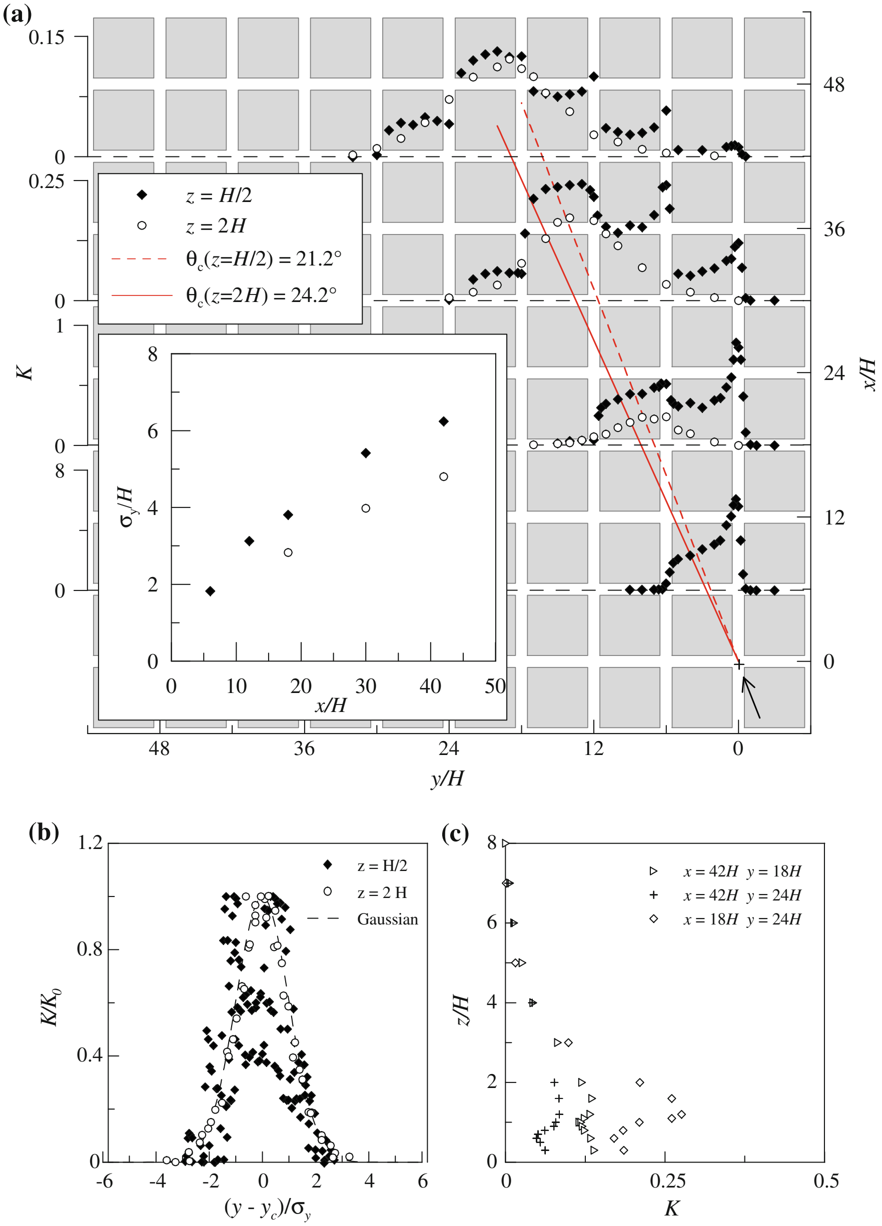

Fig. 12 Plume behaviour throughout the array, $\theta = 27.5°$—*Configuration* 1. **a** Horizontal mean concentration profiles at various positions downwind of the source (+) within and above the array. In the window, the spatial evolution of the horizontal plume spreading is shown. **b** Normalised horizontal mean concentration profiles compared to the unitarian Gaussian, and **c** vertical mean concentration profiles at various positions downstream the source

4.2.3 $\theta = 47.5°$

For $\theta = 47 \pm 2.5°$, the horizontal profiles of the normalised mean concentration are presented in Fig. 13a. The profiles within the array have a similar shape to that measured for $\theta = 27.5°$, characterised by approximately constant values within the streets and sharp gradients at the intersections. The symmetry of this configuration with respect to the diagonal of the array induces more symmetrical concentration profiles within the array compared to the previous cases. However the non-dimensional profiles cannot be fitted by any suitable model, while those above the array are well fitted by Gaussian curves, as in all other cases examined (Fig. 13b). The concentration values in the external flow are close to those within the canopy, even if the relative plume spreading in the external flow is smaller than that within the canopy, as for $\theta = 27.5°$. The direction of the plume centreline is almost the same within and above the canopy and approximately equal to the external wind direction. The vertical profiles of normalised mean concentration are shown in Fig. 13c and the same considerations presented for $\theta = 27.5°$ apply. The shape of the profiles close to the obstacle top indicates the higher diffusivity in the roughness sublayer, which induces an almost constant concentration value within it, i.e. for $H < z < 2H$. The large gradients close to the ground show that the pollutant is far from well mixed within the intersections.

The experiments for an incident angle of $\theta = 47.5 \pm 2.5°$ were also performed for a different geometrical layout of the array, in *Configuration 2*. The results, which for brevity are not presented here, show that the characteristics of the concentration field within and above the array are very similar to those observed for Configuration 1: constant concentration values within each street and abrupt variations at the intersections. The plume centreline follows approximately the external wind orientation, both within ($\theta_c = 43.5°$) and above the array ($\theta_c = 44.7°$), and the asymmetry of the layout has little effect on the centreline within the canopy. However the vertical and horizontal plume spreadings are increased compared to the previous configuration, both within and above the array. We discuss these features in the next section.

4.2.4 Comparative Discussion

To compare the results of the different configurations and to quantify the influence of the wind orientation on the behaviour of the pollutant plume we focus on three parameters: the plume centreline and the horizontal and vertical plume spreadings. To that end we need to express these quantities in a reference system common to all the cases, which is that aligned with the wind direction. If we assume $\{x, y, z\}$ as the coordinate system aligned with the streets in the array, $\{x_{\text{eff}}, y_{\text{eff}}, z\}$ as the system aligned with the wind direction, and θ the angle between the two coordinate systems, the coordinate transformations are defined as follows:

$$x_{\text{eff}} = x \cos\theta + y \sin\theta, \tag{9}$$

$$y_{\text{eff}} = -x \sin\theta + y \cos\theta. \tag{10}$$

The effective plume centreline coordinates $x_{c,\text{eff}}$ and $y_{c,\text{eff}}$ and the plume spreadings $\sigma_{y,\text{eff}}$ and $\sigma_{y,\text{eff}}$ are therefore:

$$x_{c,\text{eff}}(x/\cos\theta) = x_c \cos\theta + y_c \sin\theta, \tag{11}$$

$$y_{c,\text{eff}}(x/\cos\theta) = -x_c \sin\theta + y_c \cos\theta, \tag{12}$$

$$\sigma_{y,\text{eff}}(x/\cos\theta) = \sigma_y \cos\theta, \tag{13}$$

$$\sigma_{z,\text{eff}}(x/\cos\theta) = \sigma_z, \tag{14}$$

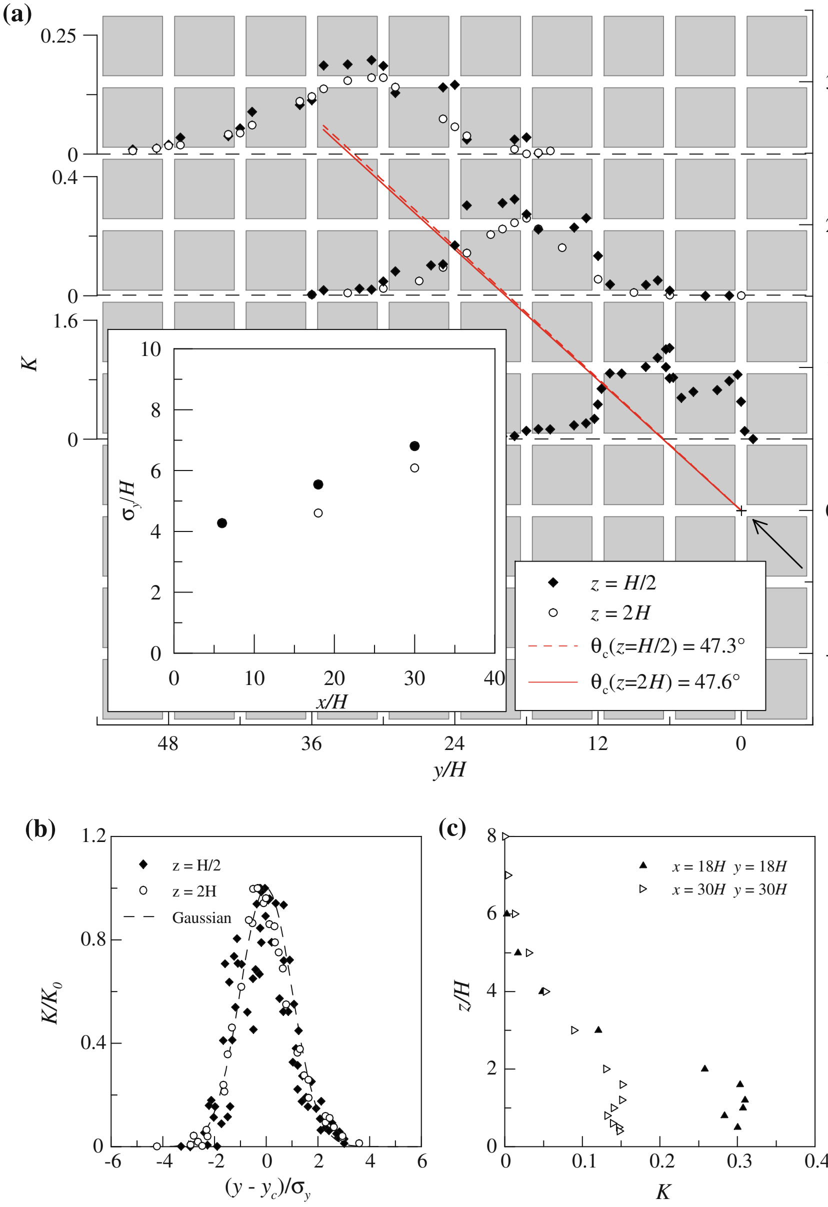

Fig. 13 Plume behaviour throughout the array, $\theta = 47.5°$—*Configuration* 1. **a** Horizontal mean concentration profiles at various positions downwind of the source (+) within and above the array. In the window, the spatial evolution of the horizontal plume spreading is shown. **b** Normalised horizontal mean concentration profiles compared to the unitarian Gaussian, and **c** vertical mean concentration profiles at various positions downstream the source

where x_c and y_c are the plume centreline coordinates in the coordinate system aligned with the axes of the streets in the array, i.e. $\{x, y, z\}$. It is worth noting that the effective plume centreline is equivalent to the effective plume deflection, i.e. the deviation of the

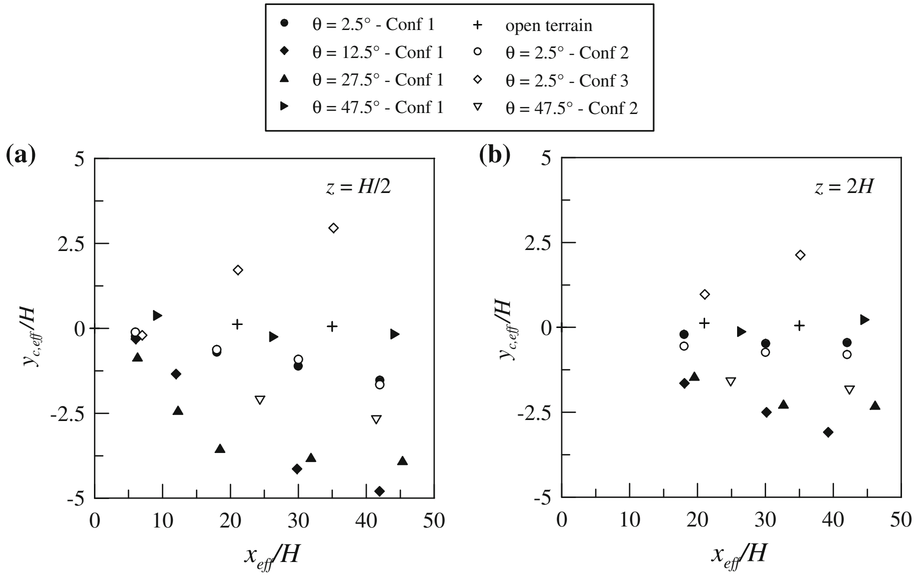

Fig. 14 Effective plume deflection within (**a**) and above (**b**) the array

plume centreline with respect to the external wind direction in the coordinate system $\{x_{\text{eff}}, y_{\text{eff}}, z\}$.

4.2.5 Plume Centreline Deflection

In Fig. 14 we plot the effective plume deflection $y_{c,\text{eff}}$ as a function of the distance downwind of the source for all the studied configurations. In Configuration 1, the deflection is close to zero for small values of θ as well as for $\theta = 47.5°$. In both cases this is due to an almost symmetric layout with respect to the axis x_{eff}. Values significantly different from zero are detected in two cases: for $\theta = 12.5°$ and $\theta = 27.5°$. A similar result was obtained by Yee and Biltoft (2004), who observed that for incident angles of approximately 20°, the centreline of the plume was deflected towards a line normal to the front face of the array. This deflection progressively reduces as θ approaches 45°. Our results also show a notable deflection of the plume in Configuration 3 when $\theta = 2.5°$. The reason for this deflection could not be identified precisely and is probably due to amplifications of instabilities due to slight asymmetries within the obstacle array (Sect. 4.1.2), as already observed by previous authors (Hoydysh and Dabberdt 1994; Robins et al. 2002), who noted how sensitive dispersion behaviour is compared to quite small departures from symmetry. These results clearly show that, even in the regular street network, the spatial evolution of the plume within the array is somehow decoupled from that in the external flow, in that θ_c within the array can depart significantly from θ.

4.2.6 Plume Spreading

The spatial evolution of the dispersion parameters $\sigma_{y,\text{eff}}$ and $\sigma_{z,\text{eff}}$ for all the configurations is plotted in Fig. 15. Since the dynamical conditions in the external boundary layer do not differ from one configuration to the other above the blending height, it is worth noting that

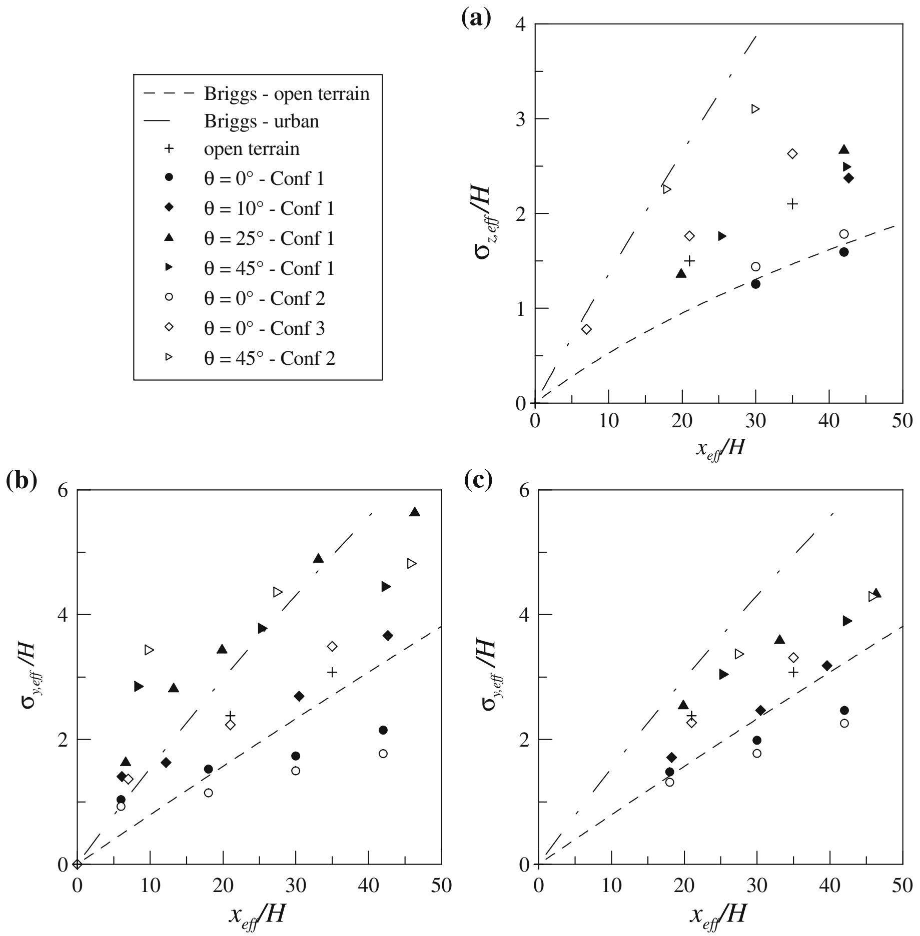

Fig. 15 Effective dispersion parameter: **a** vertical plume spreading; horizontal plume spreading within (**b**) and above (**c**) the array

the difference in the evolution of $\sigma_{y,\mathrm{eff}}$ and $\sigma_{z,\mathrm{eff}}$ is entirely due to the different dispersion patterns within the array and the roughness sublayer.

In Fig. 15a shows the non-dimensional vertical plume spreading $\sigma_{z,\mathrm{eff}}/H$ as a function of the distance from the source together with the model proposed by Briggs (1974). For all configurations $\sigma_{z,\mathrm{eff}}/H$ increases with increasing θ. The differences in $\sigma_{z,\mathrm{eff}}/H$ can be fully explained by the increased diffusivity in the roughness sublayer, whose dynamics and vertical extent differ from one case to another (Sect. 3.1). The smallest values of $\sigma_{z,\mathrm{eff}}/H$ are given by $\theta = 2.5°$ for Configuration 1 and Configuration 2, with small differences between them. In these skimming flow conditions the obstacles do not affect the flow dynamics (Salizzoni et al. 2008) and their main role is to vertically 'displace' the overlying boundary-layer. The resulting boundary-layer flow is instead determined by the smallest scale elements at the top of the obstacles and the depth of the roughness sublayer is of the same order as the size of this smallest scale roughness. Therefore, the dispersion patterns do not differ from those in open terrain conditions for a flow over a wall covered by nuts such as those placed over the obstacles. For these reasons it is not surprising that the evolution of $\sigma_{z,\mathrm{eff}}/H$ agrees well with that predicted by the Briggs' model in open terrain (Fig. 15a). When the angle θ is increased the external flow appears to be more sensitive to the geometrical configuration of the larger scale obstacles and the spacing between them, although their effect is confined by the dynamics of the roughness sublayer, within which we observed increased levels of fluctuations (Fig. 3d). The increased fluctuations, together with an increased mixing length, give rise to the enhanced spreadings observed for increasing values of θ. With the same arguments we can explain the values of $\sigma_{z,\mathrm{eff}}/H$ registered in Configuration 3 for $\theta = 2.5°$ and $\theta = 47.5°$. In these two cases, since the extent of the roughness sublayer is the same, the different $\sigma_{z,\mathrm{eff}}/H$ are entirely due to the enhanced fluctuation intensities characterising the roughness sublayer for $\theta = 47.5°$.

The evolution of the plume in the transverse direction is more difficult to interpret. Broadly speaking we observe that increased values of plume spreading within the array correspond to increased angles θ. An important exception is for $\theta = 27.5°$, whose values for $\sigma_{y,\mathrm{eff}}/H > 30$ exceed those observed for $\theta = 47.5°$. Analysis of the plot reveals that, for $\theta = 47.5°$, the plume is characterised by a very large initial value but its growth rate is almost the same as that observed for $\theta = 2.5°$, both for Configurations 1 and 2. Conversely the growth rate of $\sigma_{y,\mathrm{eff}}/H$ is significantly larger for $\theta = 12.5°$ and $\theta = 27.5°$, as well as for $\theta = 2.5°$ in Configuration 3. These results show a clear correlation between the deflection of the plume centreline and the growth rate of $\sigma_{y,\mathrm{eff}}/H$ within the canopy. The magnitude of $\sigma_{y,\mathrm{eff}}/H$ is generally smaller above the array than within it, except for low θ. We stress here that the external flow conditions are almost the same for all configurations studied and that the different dispersion patterns above the array are almost entirely due to the different spreading of the plume within the array. This induces a different spatial distribution of the vertical mass fluxes at the interface of the canopy/atmosphere and therefore different spreading of the plume in the external flow.

Finally we compare our results with the model proposed by Briggs (Britter and Hanna 2003), which is commonly used as a reference in several pollutant dispersion models. The relations of the Briggs' model are given in Table 3 for neutral stability conditions. This model was largely based on the St. Louis dispersion study (McElroy and Pooler 1968), in which the buildings were characterised by non-uniform height and probably smaller W/H ratios. For this reason we do not present a detailed discussion on the differences between the model and our results, obtained for an idealised urban geometry. There is one feature however that we wish to point out. The comparison shows that the Briggs' urban dispersion model overestimates in large part the plume spreading for the configuration studied, except for $\sigma_{y,\mathrm{eff}}/H$ for $\theta = 27.5°$ and $\theta = 47.5°$. The formulae proposed by Briggs assume that the presence of an urban area induces larger plume spreadings, for any incident wind direction, compared to those for dispersion in open terrain. However, our results show that the spreading of a dispersing plume within our idealised urban canopy is not necessarily enhanced compared to that in open terrain and strongly depends on the incident wind direction. This is an important feature that characterises the pollutant dispersion in these typical 'dense' and regular geometries, in contrast to what is commonly observed in sparse obstacle arrays.

5 Conclusion

We have investigated the dispersion of a passive tracer in an idealised urban district. For that purpose we performed wind-tunnel experiments for a street network, made up of regularly spaced and densely packed obstacles. The relative position of the obstacles and their

Table 3 Briggs' interpolation formulae for neutral stability conditions

	σ_y	σ_z
Open terrain	$0.08x(1+0.0001x)^{-1/2}$	$0.06x(1+0.0015x)^{-1/2}$
Urban areas	$0.16x(1+0.0004x)^{-1/2}$	$0.14x(1+0.0003x)^{-1/2}$

orientation were varied. The experiments have therefore been performed for different configurations in order to study the influence of the geometrical layout and of the wind direction.

The street network was overlain by an atmospheric boundary-layer flow in neutral conditions. The experimental conditions were arranged in order to obtain almost identical conditions in a large part of the external flow, for all configurations studied. The only relevant differences were concentrated close to the obstacle top in the roughness sublayer.

The influence of the geometrical layout and wind direction on the plume behaviour throughout the array has been investigated focusing on :

- the turbulent mass exchanges at the street intersections;
- the advection along the street axes;
- the mass transfer at the top of the canopy.

The mass exchanges at the street intersection cause the plume to spread in the horizontal plane, happening for all geometrical layouts and wind directions. The intensity of the mass fluxes at the intersection depends on the street aspect ratio and increases with increasing wind direction.

The role of advection along the street axes acts differently on plume spreading, depending on the geometrical layout and wind directions. For low θ its effect is to confine the plume within the street in which it has been emitted, resulting in a reduced spreading of the plume compared to that observed in open terrain. This effect, referred to as 'channelling', is almost insensitive to S_y/H, the aspect ratio of the street parallel to the wind direction, whereas it is very sensitive to S_x/H, the aspect ratio of the perpendicular street. Conversely, for larger angles of the external wind direction, the advection along the street axes results in increased plume spreading. From our results we infer that this occurs for directions larger than a critical value between $\theta = 12°$ and $\theta = 27.5°$.

The transfer at the top of the canopy appears highly inhomogeneous in the horizontal plane. In particular our experiments show that the vertical transfer is higher within streets whose axes are more deflected relative to the wind direction. The magnitude of the vertical exchange velocity is reduced compared to that related to the mean advection along the street axes. The tracer concentrations are therefore almost uniform in each street section (between two intersections), except for low θ, when the mean advective transfer in the transverse streets is almost zero.

It is worth noting that dense and regular geometries investigated here differ from those of most previous experiments in idealised urban districts comprised of equally regular but sparse obstacle arrays (e.g. MacDonald et al. 1997; Yee and Biltoft 2004; Gailis and Hill 2006). Therefore, the present results show important differences from those obtained in sparse canopies. Firstly, the horizontal plume spreading in these arrays is not necessarily enhanced compared to that in open terrain. Secondly, the direction of the plume centreline can be significantly deflected from the external wind direction. Finally, the horizontal plume spreading and its growth rate can be very different within and above the array and depend strongly on the relative direction of the external wind. We believe that these are important features characterising pollutant dispersion in typical urban geometries, and should be taken into account in dispersion models at the district scale.

Acknowledgements The authors would like to express their gratitude to A. Ezzamel for carefully reading the manuscript and providing a critical review of its content. The first author was supported by Regione Piemonte via the project "AirToLiMi: Modelling and simulating sustainable mobility strategies. A study of three real test cases: Turin, Lyon, Milan" (CIPE 2006).

References

Antonia RA, Luxton R (1971) The response of a turbulent boundary layer to a step change in surface roughness. Part 1: smooth to rough. J Fluid Mech 48(4):721–761

Assimakopoulos VD, Apsimon HM, Moussiopoulos N (2003) A numerical study of atmospheric pollutant dispersion in different two-dimensional street canyon configurations. Atmos Environ 37(29):4037–4049

Belcher S, Jerram N, Hunt J (2003) Adjustment of a turbulent boundary layer to a canopy of roughness elements. J Fluid Mech 488:369–398

Briggs GA (1974) Diffusion estimates for small emissions. USEAC Rep, ATDL-106 83-145. Air Resource Atmospheric Turbulence and Diffusion Laboratory, Oak Ridge, USA

Britter R, Hanna S (2003) Flow and dispersion in urban areas. Annu Rev Fluid Mech 35:469–496

Buccolieri R, Sandberg M, Di Sabatino S (2010) City breathability and its link to pollutant concentration distribution within urban-like geometries. Atmos Environ. doi:10.1016/j.atmosenv.2010.02.022

Coceal O, Thomas TG, Castro IP, Belcher S (2006) Mean flow and turbulence statistics over groups of urban-like cubical obstacles. Boundary-Layer Meteorol 121:491–519

Davidson M, Mylne K, Jones C, Phillips J, Perkins R, Fung J, Hunt J (1995) Plume dispersion through large groups of obstacles—a field investigation. Atmos Environ 29(22):3245–3256

Davidson MJ, Snyder WH, Lawson RE, Hunt JCR (1996) Wind tunnel simulations of plume dispersion through groups of obstacles. Atmos Environ 30(22):3715–3731

Dobre A, Arnold S, Smalley R, Boddy J, Barlow J, Tomlin A, Belcher J (2005) Flow field measurements in the proximity of an urban intersection in London, UK. Atmos Environ 39:4647–4657

Fackrell JE, Robins AG (1982) Concentration fluctuations and fluxes in plumes from point sources in aturbulent boundary layer. J Fluid Mech 117:1–26

Gailis RM, Hill A (2006) A wind tunnel simulation of plume dispersion within a large array of obstacles. Boundary-Layer Meteorol 119:289–338

Garbero V (2008) Pollutant dispersion in urban canopy. PhD thesis, Politecnico di Torino—Ecole Centrale de Lyon, 153 pp

Garbero V, Salizzoni P, Soulhac L, Mejean P (2011) Measurements and CFD simulations of flow and dispersion in urban geometries. Int J Environ Pollut 44 (to appear)

Goode K, Belcher SE (1999) On the parameterisation of the effective roughness length for momentum transfer over heterogeneous terrain. Boundary-Layer Meteorol 93:133–154

Grimmond CSB, Oke TR (1999) Aerodynamic properties of urban areas derived from analysis of surface form. J Appl Meteorol 38(9):1262–1292

Gromke C, Ruck B (2007) Influence of trees on the dispersion of pollutants in an urban street canyon-experimental investigation of the flow and concentration field. Atmos Environ 41(16):3287–3302

Hanna SR, Tehranian S, Carissimo B, Macdonald RW, Lohner R (2002) Comparisons of model simulations with observations of mean flow and turbulence within simple obstacle arrays. Atmos Environ 36: 5067–5079

Hoydysh WG, Dabberdt WF (1994) Concentration fields at urban intersections: fluid modeling studies. Atmos Environ 28(11):1849–1860

Hoydysh WG, Dabberdt WF, Schorling M, Yang F, Holynskyj O (1995) Dispersion modeling at urban intersections. Sci Total Environ 169:93–102

Hunt A, Castro IP (1984) Scalar dispersion in model building wakes. J Wind Eng Ind Aerodyn 17:89–115

Irwin HPAH (1981) The design of spires for wind simulation. J Wind Eng Ind Aerodyn 7:361–366

MacDonald RW, Griffiths RF, Cheah SC (1997) Field experiments of dispersion through regular arrays of cubic structures. Atmos Environ 31(6):783–795

MacDonald RW, Griffiths RF, Hall DJ (1998) A comparison of results from scaled field and wind tunnel modelling of dispersion in arrays of obstacles. Atmos Environ 32(22):3845–3862

McElroy J, Pooler F (1968) St. Louis dispersion study volume II—analysis. Tech. rep., U.S. Department of Health, Education and Welfare, Arlington, VA

Oke TR (1988) Street design and urban canopy layer climate. Energy Build 11:103–113

Princevac M, Baik J, LI X, Pan H, Park S (2009) Lateral channelling within rectangular arrays of cubical obstacles. J Wind Eng Ind Aerodyn. doi:10.1016/j.jweia.2009.11.001

Raupach MR, Thom AS, Edwards I (1980) A wind-tunnel study of turbulent flow close to regularly arrayed rough surfaces. Boundary-Layer Meteorol 18:373–397

Raupach MR, Antonia R, Rajoplan S (1991) Rough-wall turbulent boundary layers. Appl Mech Rev 44(1): 1–25

Raupach MR, Hughes DE, Cleugh HA (2006) Momentum absorption in rough-wall boundary layers with sparse roughness elements in a random and clustered distributions. Boundary-Layer Meteorol 120: 201–218

Robins A, Savory E, Scaperdas A, Grigoriadis D (2002) Spatial variability and source-receptor relations at a street intersection. Water Air Soil Pollut Focus 2:381–393

Salizzoni P (2006) Mass and momentum transfer in urban boundary layer. PhD thesis, Politecnico di Torino—Ecole Centrale de Lyon, 186 pp

Salizzoni P, Soulhac L, Mejean P, Perkins R (2008) Influence of a two-scale surface roughness on a neutral turbulent boundary layer. Boundary-Layer Meteorol 127(1):97–110

Salizzoni P, Soulhac L, Mejean P (2009a) Street canyon ventilation and atmospheric turbulence. Atmos Environ 43:5056–5067

Salizzoni P, Van Liefferinge R, Soulhac L, Mejean P, Perkins R (2009b) Influence of wall roughness on the dispersion of a passive scalar in a turbulent boundary layer. Atmos Environ 43(3):734–748

Santiago JL, Martilli A (2007) CFD simulation of airflow over a regular array of cubes. Part I: three dimensional simulation of the flow and validation with wind-tunnel measurements. Boundary-Layer Meteorol 122:609–634

Sini JF, Anquentin S, Mestayer P (1996) Pollutant dispersion and thermal effects in urban street canyons. Atmos Environ 30(15):2659–2677

Snyder W (1981) Guidelines for fluid modelling of atmospheric diffusion. Report no. EPA-600/8-81-009. U.S. Environmental Protection Agency, Environmental Sciences Research Laboratory, Research Triangle Park, NC

Snyder W (1992) Some observations of the influence of stratification on diffusion in building wakes. IMA Conf: on stably stratified flows. University of Surrey, Guildford

Solazzo E, Cai X, Vardoulakis S (2008) Modelling wind flow and vehicle-induced turbulence in urban streets. Atmos Environ 42(20):4918–4931

Soulhac L (2000) Modélisation de la dispersion atmosphérique à l'intérieur de la canopéeurbaine. PhD thesis, Ecole Centrale de Lyon, 351 pp

Soulhac L, Perkins RJ, Salizzoni P (2008) Flow in a street canyon for any external wind direction. Boundary-Layer Meteorol 126:365–388

Soulhac L, Garbero V, Salizzoni P, Mejean P, Perkins R (2009) Flow and dispersion in street intersections. Atmos Environ 43:2981–2996

Tennekes H, Lumley JL (1972) A first course in turbulence. MIT Press, Cambridge, 300 pp

Theurer W, Plate EJ, Hoeschele K (1996) Semi-empirical models as a combination of wind tunnel and numerical dispersion modeling. Atmos Environ 30:3583–3597

Yee E, Biltoft CA (2004) Concentration fluctuation measurements in a plume dispersing through a regular array of obstacles. Boundary-Layer Meteorol 111:363–415